Current Applied Physics 61 (2024) 115–120

Contents lists available at ScienceDirect

Current Applied Physics

journal homepage: www.elsevier.com/locate/cap

Evaluation of vapor pressure of MoO_2Cl_2 and its initial chemical reaction on a SiO_2 surface by *ab initio* thermodynamics

Hyun-Kyu Kim, Na-Young Lee, Yeong-Cheol Kim *

School of Energy Materials and Chemical Engineering, KoreaTech, Cheonan, 31253, South Korea

ARTICLE INFO

Keywords:
MoO_2Cl_2
SiO_2
Atomic layer deposition
Vapor pressure
Surface reaction
ab initio thermodynamics

ABSTRACT

The vapor pressure of MoO_2Cl_2 and its initial chemical reaction on a SiO_2 surface were evaluated and analyzed using *ab initio* thermodynamics. The vapor pressure of MoO_2Cl_2 was calculated using the Gibbs free energy, while considering the zero-point energy, temperature-dependent enthalpy change, and entropy. The initial surface reaction was also studied as functions of temperature and partial pressure. The calculated sublimation temperature of MoO_2Cl_2 was 410 K, and its vapor pressure at 350 K was 8.2 torr. The partial pressure calculated for MoO_2Cl_2 agreed reasonably well with the experimentally measured value. The surface reaction energy barrier between MoO_2Cl_2 and SiO_2 was 0.8 eV.

1. Introduction

Three-dimensional (3D) NAND flash is a key technology in modern storage devices because of its higher memory density and lower cost compared with planar NAND [1,2]. W, with its reasonable electrical resistivity and high thermal stability, is frequently used as the word line (WL) for NAND flashes [3–5]. WF_6 is used to deposit the W WL by chemical vapor deposition (CVD); however, its byproduct, HF, etches the surrounding SiO_2 dielectric. This etching problem is alleviated using WCl_6 [6,7]. However, the structural stress caused by the increase in the number of stacks imposes a physical limit on the total stack height [8]. To overcome this, the thicknesses of the dielectric and WL must be reduced. However, the W precursors for CVD show a degraded filling performance with a decrease in thickness. WF_6 and WCl_5 have been used to improve the filling performance via atomic layer deposition (ALD) [9,10]. Additionally, the electrical resistance of the W WL increases owing to electron scattering from the surfaces and interfaces at a narrow linewidth because of its high electron mean free path (MFP) [11]. Thus, W should be replaced with other metals that have a lower bulk resistance and good filling performance.

Mo, Co, and Ru are all suitable alternatives to W, and Mo is particularly attractive because of its low cost. Mo has lower bulk resistivity and MFP than W (Mo vs W; 5.2 vs 5.6 μΩcm; 11.2 vs 15.5 nm) [12–14]. MoO_2Cl_2 is a promising precursor for the deposition of Mo thin films via CVD and ALD. It has a faster deposition rate than $MoCl_5$, a commonly used Mo precursor [15–18]. MoO_2Cl_2 shows better filling performance, forms a thin film with lower resistivity, and is less aggressive toward the barrier material TiN than other Mo precursors. In addition, MoO_2Cl_2 shows a higher vapor pressure than other Mo precursors [19], which makes it easier to transport into the reaction chamber [17]. Although experimental studies have provided valuable insights into the deposition properties of Mo precursors and the characterization of thin films, they are not only time-consuming but also resource-intensive. Simulations can be employed to reduce the effort required to identify appropriate precursors for ALD.

Yang et al. predicted the sublimation temperature and vapor pressure of various solid materials using the chemical potentials of the gas and solid phases [20], and Goel et al. calculated vapor pressure using a first-principles Monte Carlo method by predicting structural properties such as the density of liquid-state materials [21]. The chemical reaction of the precursors on the surface is also an important factor in the ALD process. The physisorption of the precursor to the surface from the gas-phase, transition from physisorption to chemisorption, chemisorption, and desorption of the byproduct were simulated by calculating the DFT electron energies for each state [22–29]. However, this method does not consider the energy variation due to experimental conditions, such as the temperature and partial pressures of the precursor and byproduct. Recently, Kang employed the Gibbs free energy for two reaction pathways between tetrakis(dimethylamino) silane (TDMAS) and a SiO_2 surface by calculating the enthalpy and entropy of the precursor and surface at $P = 1$ atm [30]. Yu et al. compared the reactions between several silicon tetrahalide precursors and the Si surface using the Gibbs

* Corresponding author.
E-mail address: yckim@koreatech.ac.kr (Y.-C. Kim).

https://doi.org/10.1016/j.cap.2024.02.016
Received 6 November 2023; Received in revised form 16 February 2024; Accepted 29 February 2024
Available online 1 March 2024

free energy at $T = 623$ K and $P = 1.5$ torr [31]. Weckman et al. analyzed the Gibbs free energy and rate constant for the reaction between trimethylaluminum (TMA) and an Al_2O_3 surface at $T = 298$ and 450 K and $P = 0.015$ torr [32]. However, to the best of our knowledge, there have been few ALD simulation studies on evaluation of vapor pressure of Mo precursors and their surface reactions [33].

In this report, we studied the vapor pressure of MoO_2Cl_2 using the Gibbs free energy of the solid and gas phases, and its initial chemical reaction on a H-terminated β-SiO_2 (111) surface. The reaction process was divided into gas-phase, physisorption, transition from physisorption to chemisorption, chemisorption, and desorption states. The evaluation of vapor pressure and surface reaction can be applied to screen many potential precursors in a very cost-efficient manner.

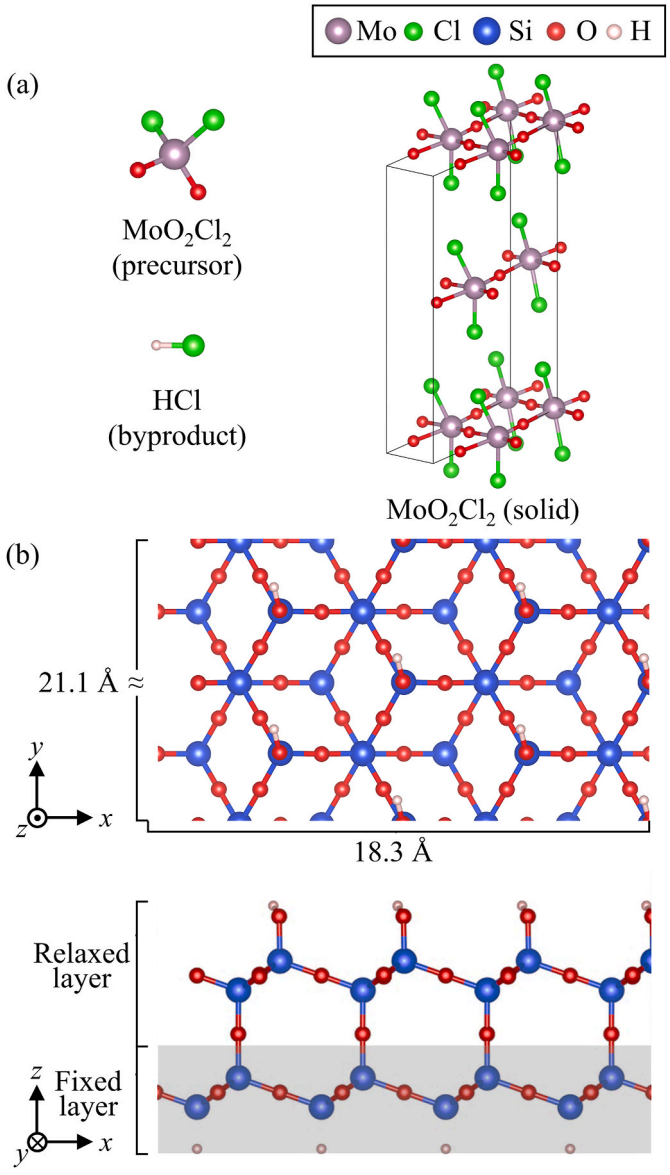

Fig. 1. (a) MoO_2Cl_2 (precursor), HCl (byproduct), and crystal structure of MoO_2Cl_2 in the solid phase (space group Cc). (b) Top and side views of H-terminated β-cristobalite SiO_2 (111) surface. The area of the constructed surface was 18.3 × 21.1 Å^2. The atoms in the gray region of side view are fixed to simulate bulk β-cristobalite SiO_2. A vacuum of 15 Å is added on the surface to reduce the interaction between the top and bottom of the surface slab.

2. Computational methods

Fig. 1 (a) shows MoO_2Cl_2, HCl, and solid MoO_2Cl_2 [34,35]. MoO_2Cl_2 and HCl are shown as the precursor and byproduct, respectively, because MoO_2Cl_2 reacts with the H-terminated SiO_2 surface to produce HCl. The HCl production will be discussed in the following section. A volume of 15 × 15 × 15 Å^3 was used to optimize the precursor and byproduct molecules to balance the calculation time and accuracy due to the periodic boundary conditions in DFT. The lattice parameters of the solid MoO_2Cl_2 (space group Cc) were $a = 14.3$, $b = 4.0$ and $c = 7.8$ Å with $\beta = 105.4°$. A model of a SiO_2 surface slab was constructed from the β-cristobalite SiO_2 structure. When the structure is cut along the (111) plane, the Si–O–Si layer and the O layer on top become the basic repeating units along the [111] direction. Two units were stacked in the surface-slab model. β-cristobalite SiO_2 with similar density and band structure to amorphous SiO_2 was used to construct the surface model [36]. Fig. 1 (b) shows the top and side views of the surface shown along the $[00\bar{1}]$ and [010] directions, respectively. The area of the constructed surface was 18.3 × 21.1 Å^2. The H atoms were attached to the surface O atoms to simulate the carrier gas H_2 used in the ALD process. To avoid the formation of dangling bonds when simulating the bulk structure, H atoms were attached to the bottom Si atoms [22]. In addition, a vacuum of 15 Å was added to reduce the interaction between the slab surface and the slab bottom, and the slab bottom in the gray area of the figure was fixed to simulate bulk [22–29].

Table 1 lists the equations used to calculate the Gibbs free energy (G) of each surface reaction state. G was calculated using the equation $G = H - TS$, where H is the enthalpy, T is the temperature, and S is the entropy. H is represented by the sum of the DFT electron energy (E), the zero-point energy (ZPE), and the temperature-dependent enthalpy change ($\int C_p dT$). The entropies due to translation, rotation, and vibration of molecules were calculated using the Sackur-Tetrode equation, rigid-rotor model, and harmonic oscillation, respectively [30–32,37–39]. For the surface slab and bulk crystal, the entropy due to vibration was calculated. The degrees of freedom (DOF) for the vibration frequencies were $3N$–6 and $3N$–5 for the nonlinear and linear molecules, respectively, where N = number of atoms [37–39]. The solid phase and surface reaction states both limit translational and rotational freedom, so all degrees of freedom were considered except for the virtual frequencies of the atoms considered in the calculations. All vibration frequencies below 50 cm^{-1} were also set to 50 cm^{-1} to compensate for the abnormal correction in the results due to the small vibration frequencies [40]. The equation for entropy due to translation was used to consider the partial

Table 1
Equations for the free energy calculations [30–32,37,39].

Equation	Notation
$H = E + \text{ZPE} + \int C_p dT$	H: enthalpy E: DFT electron energy ZPE: zero-point energy $\int C_p dT$: temperature-dependent enthalpy change
$G = H - TS$	G: free energy S: entropy
$S = S_t + S_r + S_v$	S_t: translational S S_r: rotational S S_v: vibrational S
$S_t = k_B\left[\ln\left[\left(\frac{2\pi m k_B T}{h^2}\right)^{3/2}\frac{k_B T}{P}\right] + \frac{5}{2}\right]$	k_B: Boltzmann constant m: mass of molecule h: Planck's constant P: partial pressure of molecule
$S_r = k_B\left[\ln\left[\left(\frac{8\pi^2 k_B T}{h^2}\right)^{3/2}\frac{\sqrt{\pi I_A I_B I_C}}{\sigma}\right] + \frac{3}{2}\right]$	I_A, I_B, I_C: principal moments of inertia σ: symmetry number of molecule
$S_v = k_B\sum_i^{DOF}\left[\frac{h\omega_i}{k_B T(e^{h\omega_i/k_B T}-1)} - \ln(1-e^{-h\omega_i/k_B T})\right]$	DOF: degree of freedom ω_i: ith angular frequency

pressures of the precursor and byproduct. σ represents the symmetry number of the molecules (2 and 1 for MoO_2Cl_2 (C_{2v}) and HCl ($C_{\infty v}$), respectively) [38]. The symbol in parentheses is the point group of each molecule.

The vapor pressure was calculated using G in the solid and gas structures of the precursor. The sublimation temperature (T_{sub}) of the precursor was obtained when $G_{gas} = G_{solid}$ at $P = 1$ atm, where G_{gas} and G_{solid} are the G values for the gas and solid phases of the precursor, respectively. The vapor pressure at a given temperature was calculated under the same conditions. The surface reaction calculations were divided into five surface reaction states based on weak bonds in the precursor and surface. Bond dissociation energy (BDE) was calculated to find out the weak bonds in the precursor and surface. In the case of Mo–Cl in MoO_2Cl_2, its BDE is the energy difference between two radicals (MoO_2Cl and Cl) and MoO_2Cl_2. The following surface reaction states were calculated: gas-phase (gas), physisorption (phys), transition (tran), chemisorption (chem), and desorption (des).

gas-phase (gas): (SiO_2)–O–H + MoO_2Cl_2

physisorption (phys): (SiO_2)–O–H ⋯ MoO_2Cl_2

transition (tran): (SiO_2)–O ⋯ H ⋯ Cl ⋯ MoO_2Cl

chemisorption (chem): (SiO_2)–O–MoO_2Cl ⋯ HCl

desorption (des): (SiO_2)–O–MoO_2Cl + HCl,

where "+" in (SiO_2)–O–H + MoO_2Cl_2 represents OH-terminated SiO_2 surface with a distant MoO_2Cl_2, and " …" represents the physisorbed or half-chemisorbed state of precursor or byproduct to surface.

All the DFT calculations were performed using the Vienna *ab initio* simulation package (VASP) [42,43], and the projector-augmented wave method was employed to handle the electron wave function [44,45]. The exchange-correlation energy was calculated using the Perdew-Burke-Ernzerhof (PBE) method [46]. The K-point mesh was sampled on $1 \times 4 \times 2$, $2 \times 2 \times 2$, and $1 \times 1 \times 1$ Monkhorst-Pack grids for the solid MoO_2Cl_2, the surface slab, and molecules, respectively [47]. The van der Waals dispersion energy correction was considered using the DFT-D3 method presented by Grimme et al. [48]. Both the electrons and structures were optimized until the total energy difference was less than 10^{-3} eV and 10^{-2} eV, respectively. The ZPE and temperature-dependent enthalpy change ($\int C_p dT$) were calculated using vibrational frequency [37–39]. The vibration frequencies of each structure were calculated using the finite displacement method. The results of the H, S, and G calculations were compared to those obtained using VASPKIT software [40].

3. Results and discussion

Table 2 shows the bond length and BDE of Mo–O, Mo–Cl, Si–O, and O–H bonds in MoO_2Cl_2 and the H-terminated SiO_2 surface. From BDE, Mo–Cl is weaker than Mo–O in MoO_2Cl_2, and O–H is weaker than Si–O in the surface. Therefore, the surface reaction between MoO_2Cl_2 and H-terminated SiO_2 surface is predicted to occur by breaking Mo–Cl and O–H to produce HCl. This prediction was confirmed by the experiment, which showed an increase in the partial pressure of HCl during the reaction between MoO_2Cl_2 and the surface [41].

Table 2
Bond length and bond dissociation energy (BDE) of Mo–Cl, Mo–O, Si–O, and O–H bonds in MoO_2Cl_2 and the SiO_2 surface. The surface reaction is predicted to form HCl by the dissociation of Cl in the precursor and H in the SiO_2 surface.

	MoO_2Cl_2		H-terminated β-SiO_2 (001) surface	
	Mo–Cl	Mo–O	Si–O	O–H
Bond length (Å)	2.26	1.69	1.64	0.97
BDE (eV)	4.5	7.3	5.8	5.3

Table 3 shows the thermodynamic correction factors, such as ZPE, $\int C_p dT$, and TS for MoO_2Cl_2 (solid and gas), HCl (gas), and the surface slabs calculated at $T = 800$ K, which is a typical experimental temperature [14–17,19], and $P = 1$ atm. The changes in S_t and S_r were negligible in the solid precursor and surface slabs. ZPE, $\int C_p dT$, and TS_v increased with the number of atoms for vibrational calculation, implying that MoO_2Cl_2 has larger ZPE, $\int C_p dT$, and TS_v because it is composed of more atoms than HCl. MoO_2Cl_2 (solid) demonstrated higher degrees of freedom than MoO_2Cl_2 (gas); that is, more frequencies were considered in vibration calculation for ZPE, $\int C_p dT$, and TS_v [36–38]. TS_t increased proportionally to molecular mass, owing to which MoO_2Cl_2 demonstrated a higher value of TS_t than HCl. TS_r was determined by the moment of inertia and the symmetry number of the molecule; therefore, simple linear HCl showed a lower value of TS_r than nonlinear MoO_2Cl_2. The effect of the pressure on TS_t is discussed further in the following paragraphs.

Fig. 2 (a) shows the relative G of MoO_2Cl_2 as a function T, with the G of solid MoO_2Cl_2 at $T = 0$ K used as a reference. The vertical dashed line represents the sublimation temperature (T_{sub}) of MoO_2Cl_2 (410 K). The experimental T_{sub} was 430 K with an error of approximately 5 % [19]. Fig. 2 (b) shows the calculated vapor pressure (P_{vap}) as a function of T. The canister containing the MoO_2Cl_2 source was typically heated to approximately 350 K during the deposition [41]. The P_{vap} at 350 K was calculated to be 8.2 torr, and experimentally measured value was 3.3 torr. This vapor pressure evaluation procedure can be applied to screen many potential precursors in a very cost-efficient manner. This finite displacement supercell approach offers a relatively simple and widely accessible method for phonon calculations, but a large supercell should be used to sample as many phonon modes at Γ as possible to improve its accuracy as mentioned in Ref. [49].

Fig. 3 shows the DFT electron energy ($\Delta E_{des} = E_{des} - E_{gas}$) and Gibbs free energy ($\Delta G_{des} = G_{des} - G_{gas}$) for desorption relative to the gas-phase state. G_{gas} was obtained at T = 800 K and $P_{MoO_2Cl_2} = 1$ torr. The blue and light red bars and the dark red bar represent ΔE and ΔG for $P_{HCl} = 1$ (ΔG^{I}_{des}) and 10^{-6} torr (ΔG^{II}_{des}), respectively. The negative ΔE indicates that the initial reaction of MoO_2Cl_2 with H-terminated β-SiO_2 (111) surface is exothermic, whereas the positive ΔG^{I}_{des} indicates that the reaction is endergonic. This is because the entropy of MoO_2Cl_2 increases more than that of HCl with increasing temperature, as reported by Kang's paper [30]; see gas-phase and desorption states in Table 3. However, the partial pressure of the byproduct after the reaction may be significantly lower than that of the precursor delivered from the canister. $P_{HCl} = 10^{-6}$ torr was used to account for the low consumption of the precursor in the reaction. ΔG^{II}_{des} became lower than ΔG^{I}_{des} because S_t of HCl increased with the decrease in P_{HCl}. These results indicate that MoO_2Cl_2 spontaneously reacts with the SiO_2 surface when the gas-phase and desorption states are considered among the five states. The five states are discussed in the following paragraph.

Fig. 4 shows the DFT electron energy (ΔE) and Gibbs free energy (ΔG) for five states relative to the gas-phase state. G_{gas} was obtained again at $T = 800$ K and $P_{MoO_2Cl_2} = 1$ torr. The relative DFT electron energy for physisorption ($E_p = E_{phys} - E_{gas}$) of MoO_2Cl_2 was −0.75 eV, whereas the relative Gibbs free energy for physisorption ($G_p = G_{phys} - G_{gas}$) was 1.53 eV. When a molecule physisorbs onto a surface, TS_t and TS_r become negligible, causing an abrupt G_{phys} increase. This increase in G_p has also been observed in other studies [30,31]. The DFT electron energy for activation ($E_a = E_{tran} - E_{phys}$) was 0.91 eV, while the Gibbs free energy for activation ($G_a = G_{tran} - G_{phys}$) was 0.80 eV. Unlike the previous trend between E_p and G_p, G_a varied insignificantly from E_a because G increased at a similar rate in both the physisorption and transition states (see Table 3). Therefore, the evaluation of the activation energy using the DFT electron energy is preferable because of its low computational cost. MoO_2Cl_2 showed a reverse activation DFT electron energy ($E_r = E_{tran} - E_{chem}$) of 0.69 eV, which was smaller than E_a. The reverse activation Gibbs free energy ($G_r = G_{tran} - G_{chem}$) was 0.79 eV

Table 3
Calculated thermodynamic correction factors (ZPE, $\int C_p dT$, and TS) at $T = 800$ K and $P = 1$ atm. The units are eV.

System		$H - E$		TS		
		ZPE	$\int C_p dT$	TS_t	TS_r	TS_v
MoO_2Cl_2 (solid)		0.27	0.80	–	–	2.29
MoO_2Cl_2 (gas)		0.24	0.70	1.62	1.04	0.96
HCl (gas)		0.18	0.24	1.44	0.34	0.00
(SiO_2)–O–H		0.37	0.23	–	–	0.52
(SiO_2)–O–MoO_2Cl		0.32	0.64	–	–	1.58
(SiO_2)–O–H + MoO_2Cl_2	**(gas-phase)**	0.61	0.93	1.62	1.04	1.48
(SiO_2)–O–H···MoO_2Cl_2	**(physisorption)**	0.63	0.91	–	–	2.31
(SiO_2)–O···H···MoO_2Cl···Cl	**(transition)**	0.52	0.91	–	–	2.30
(SiO_2)–O–MoO_2Cl···HCl	**(chemisorption)**	0.52	0.90	–	–	2.38
(SiO_2)–O–MoO_2Cl + HCl	**(desorption)**	0.50	0.88	1.44	0.34	1.58

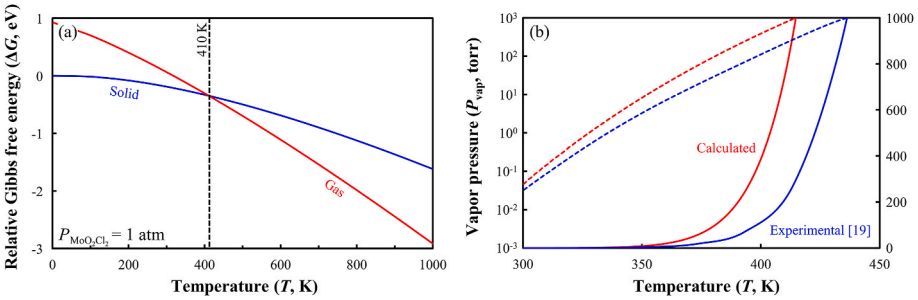

Fig. 2. (a) Relative Gibbs free energy (G) of solid (blue) and gas (red) MoO_2Cl_2 at $P_{MoO_2Cl_2} = 1$ atm. G of solid MoO_2Cl_2 at $T = 0$ K is used as a reference. The vertical dashed line indicates the sublimation temperature ($T_{sub} = 410$ K). (b) Vapor pressure as a function of T. The solid and dashed curves show linear and logarithmic scales of the vapor pressure, respectively. The red and blue curves indicate calculated and experimental vapor pressures, respectively [19]. (For interpretation of the references to colour in this figure legend, the reader is referred to the Web version of this article.)

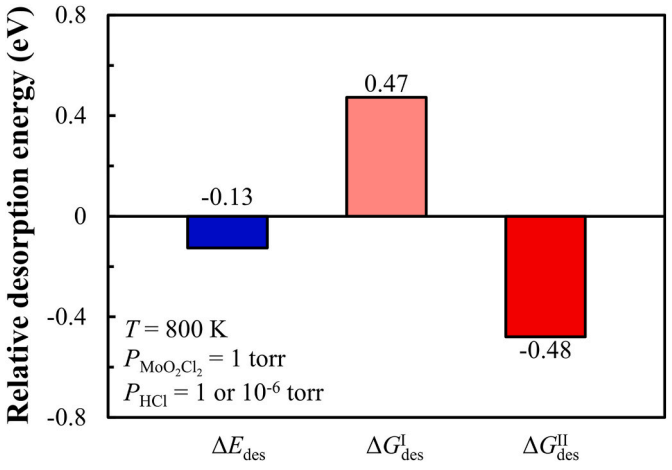

Fig. 3. Relative desorption energy ($\Delta E_{des} = E_{des} - E_{gas}$ and $\Delta G_{des} = G_{des} - G_{gas}$) of the reaction between precursor and SiO_2 surface. The blue, light red, and dark red bars indicate ΔE_{des}, ΔG_{des} for $P_{HCl} = 1$ (ΔG^{I}_{des}), and 10^{-6} torr (ΔG^{II}_{des}), respectively. The value of $P_{HCl} = 10^{-6}$ torr accounts for the fact that only a small fraction (one per million) of the delivered precursor from the canister is consumed for reaction. (For interpretation of the references to colour in this figure legend, the reader is referred to the Web version of this article.)

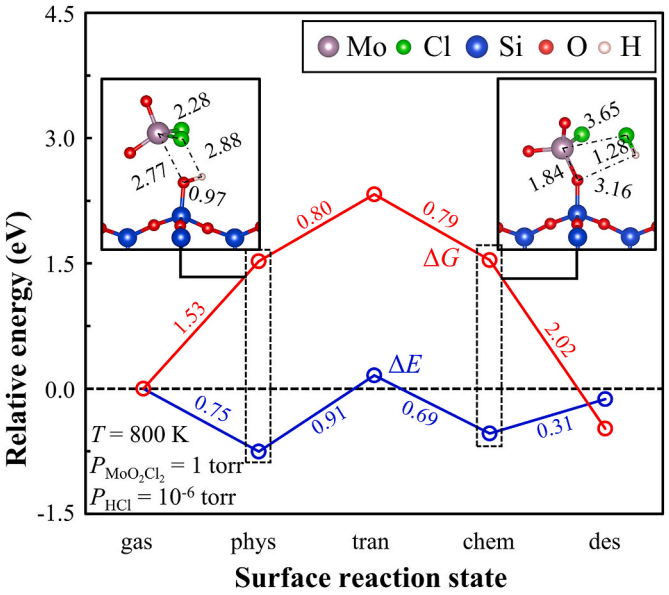

Fig. 4. Relative energy (ΔE and ΔG) of surface reaction states for MoO_2Cl_2 precursor with calculated geometries of physisorption and chemisorption states. The blue and red lines indicate ΔE and ΔG, respectively. ΔG is calculated from typical deposition process conditions ($T = 800$ K and $P_{MoO_2Cl_2} = 1$ torr). (For interpretation of the references to colour in this figure legend, the reader is referred to the Web version of this article.)

which was similar to G_a. This difference was the same as the $\int C_p dT$ and TS_v difference between chemisorption and transition states (see transition and chemisorption states in Table 3). The DFT electron energy for desorption ($E_d = E_{des} - E_{chem}$) was 0.31 eV, whereas the Gibbs free energy for desorption ($G_d = G_{des} - G_{chem}$) was −2.02 eV. This large difference occurs because the TS_t and TS_r values of the desorbed HCl are generally non-zero, but become zero when HCl is adsorbed in the chemisorption state. Therefore, the desorption process was facilitated by

the decrease in G_d resulting from the increase in TS_t. The increase of TS_t is mainly due to the desorption of HCl and decrease in P_{HCl}.

4. Conclusion

This study focused on evaluating the vapor pressure of the MoO_2Cl_2 precursor and its initial chemical reaction on the SiO_2 surface. The partial pressure calculated for MoO_2Cl_2 agreed reasonably well with the experimentally measured value. The relative Gibbs free energy was positive when the partial pressures of MoO_2Cl_2 and HCl were the same, whereas the relative Gibbs free energy became negative when a low partial pressure of HCl was considered. The physisorption of MoO_2Cl_2 on the surface from the Gibbs free energy was not favorable because of the decrease in entropy, whereas the activation energies from both the DFT energy and Gibbs free energy were almost the same. The desorption of HCl occurred easily because of the increase in entropy. Evaluation of the activation energy using the DFT electron energy alone is still feasible because of its acceptable accuracy and low computational cost.

Declaration of competing interest

The authors declare that they have no known competing financial interests or personal relationships that could have appeared to influence the work reported in this paper.

Acknowledgments

This research was supported by “Regional Innovation Strategy (RIS)" through the National Research Foundation of Korea (NRF) funded by the Ministry of Education (MOE) (2021RIS-004). This research was also supported by Education and Research Promotion Program of KOREATECH in 2022.

References

[1] A. Goda, 3-D NAND technology achievements and future scaling perspectives, IEEE Trans. Electron. Dev. 67 (2020) 1373–1381.
[2] D. Tierno, K. Croes, A. Ajaykumar, S. Ramesh, G. Van den Bosch, M. Rosmeulen, Reliability of Mo as word line metal in 3D NAND, 2021 IEEE International, Reliability Phys. Symposium (IRPS) (2021) 1–6.
[3] C. Adelmann, L.G. Wen, A.P. Peter, Y.K. Siew, K. Croes, J. Swerts, M. Popovici, K. Sankaran, G. Pourtois, S. Van Elshocht, J. Bommels, Z. Tokei, Exploring alternative metals to Cu and W for interconnects applications using automated first-principles simulations, in: IEEE International Interconnect Technol. Conference, 2014, pp. 173–176.
[4] C. Adelmann, K. Sankaran, S. Dutta, A. Gupta, S. Kundu, G. Jamieson, K. Moors, N. Pinna, I. Ciofi, S. Van Eishocht, J. Bommels, G. Boccardi, C.J. Wilson, G. Pourtois, Z. Tokei, Alternative metals: from ab initio screening to calibrated narrow line models, in: 2018 IEEE International Interconnect Technol. Conference (IITC), 2018, pp. 154–156.
[5] D. Gall, The search for the most conductive metal for narrow interconnect lines, J. Appl. Phys. 127 (2020) 050901.
[6] J.A.M. Ammerlaan, D.R.M. Boogaard, P.J. van der Put, J. Schoonman, Chemical vapour deposition of tungsten by H_2 reduction of WCl_6, Appl. Surf. Sci. 53 (1991) 24–29.
[7] F. Hirose, T. Watanabe, A. Shibata, K. Momiyama, T. Suzuki, H. Miya, Tungsten deposition by metal-chloride-reduction chemical vapor deposition, Electrochem. Solid State Lett. 14 (2011) H251–H253.
[8] A. Kruv, A. Arreghini, M. Gonzalez, D. Verreck, G. Van den bosch, I. De Wolf, A. Furnemont, Impact of mechanical stress on the electrical performance of 3D NAND, in: 2019 IEEE International Reliability Phys. Symposium (IRPS), 2019, pp. 1–5.
[9] G. Wang, Q. Xu, T. Yang, J. Luo, J. Xiang, J. Xu, G. Xu, C. Li, J. Li, J. Yan, C. Zhao, D. Chen, T. Ye, Application of atomic layer deposition tungsten (ALD W) as gate filling metal for 22 nm and beyond nodes CMOS technology, ECS Trans. 58 (2013) 317–324.
[10] M. Lee, R. Hidayat, D.K. Nandi, T.H. Kim, Y. Kim, S. Kim, W.-J. Lee, S.-H. Kim, Atomic layer deposition of tungsten and tungsten-based compounds using WCl_5 and various reactants selected by density functional theory, Appl. Surf. Sci. 563 (2021) 150373.
[11] D. Gall, The resistivity bottleneck: the search for new interconnect metals, in: 2020 International Symposium on VLSI Technol. Syst. Appl. (VLSI-TSA), 2020, pp. 112–113.
[12] H.O. Pierson, Handbook of Refractory Carbides and Nitrides, Noyes, Westwood, NJ, 1996.
[13] D. Gall, Electron mean free path in elemental metals, J. Appl. Phys. 119 (2016) 085101.
[14] E. Zoubenko, S. Iacopetti, K. Weinfeld, Y. Kauffmann, P. Van Cleemput, M. Eizenberg, Impact of chemical bonding difference of ALD Mo on SiO_2 and Al_2O_3 on the effective work function of the two gate stacks, J. Vac. Sci. Technol. A 39 (2021) 043201.
[15] T.H. Baum, Bryan C. Hendrix, Philip S.H. Chen, Robert Wright Jr., Woeckener James, Method for Forming Molybdenum Films on Substrate, 2019 US20200131628A1.
[16] T.H. Baum, Philip S.H. Chen, Robert L. Wright, Hendrix Bryan, Shuang Meng, Richard Assion, CVD Mo Deposition by Using $MoOCl_4$, 2018 US11107675B2.
[17] S. Vivek Thombare, Gorun Butail, Patrick A. Van Cleemput, Ilanit FISHER, Deposition of Pure Metal Films, 2022 US20220389579A1.
[18] S. Vivek Thombare, Raashina Humayun, Michal Danek, Chiukin Steven Lai, Joshua Collins, Bamnolker Hanna, Griffin John Kennedy, Gorun Butail, A. Patrick, Van Cleemput, Low Resistivity Films Containing Molybdenum, 2022 US20220223471A1.
[19] H.W. Gäggeler, A. Türler, Gas-phase chemistry, in: The Chemistry of Superheavy Elements, Kluwer Academic Publishers, Boston, 2003, pp. 237–289.
[20] Y. Hu, K. Wang, M. Müller, E. Wessel, R. Spatschek, Theoretical prediction of the sublimation behavior by combining ab initio calculations with statistical mechanics, Materials 16 (2023) 2826.
[21] H. Goel, S. Ling, B.N. Ellis, A. Taconi, B. Slater, N. Rai, Predicting vapor liquid equilibria using density functional theory: a case study of argon, J. Chem. Phys. 148 (2018) 224501.
[22] J.-S. Kim, J.-H. Yang, Y.-C. Jeong, D.-H. Kim, S.-B. Baek, Y.-C. Kim, Effect of amino ligand size of Si precursors on initial reaction with an –OH-terminated Si(001) surface for atomic layer deposition, Jpn. J. Appl. Phys. 53 (2014) 08NE04.
[23] S.-B. Baek, D.-H. Kim, Y.-C. Kim, Adsorption and surface reaction of bis-diethylaminosilane as a Si precursor on an OH-terminated Si (001) surface, Appl. Surf. Sci. 258 (2012) 6341–6344.
[24] Y.-C. Jeong, S.-B. Baek, D.-H. Kim, J.-S. Kim, Y.-C. Kim, Initial reaction of silicon precursors with a varying number of dimethylamino ligands on a hydroxyl-terminated silicon (001) surface, Appl. Surf. Sci. 280 (2013) 207–211.
[25] K.-Y. Kim, J.-H. Yang, D.-G. Shin, Y.-C. Kim, Initial reaction of hexachlorodisilane on amorphous silica surface for atomic layer deposition using density functional theory, J. Korean Ceram. Soc. 54 (2017) 443–447.
[26] J.-H. Yang, S.-B. Baek, Y.-C. Kim, Initial surface reaction of di-isopropylaminosilane on a fully hydroxyl-terminated Si (001) surface, J. Nanosci. Nanotechnol. 14 (2014) 7954–7960.
[27] D.-H. Kim, D.-H. Kim, Y.-C. Kim, Initial oxidation of gallium arsenide (001)–β2 (2×4) surface using density functional theory, J. Nanosci. Nanotechnol. 14 (2014) 7816–7820.
[28] D.-H. Kim, Y.-C. Kim, Initial reaction of dimethylaluminum isopropoxide with hydrogen-terminated Si (001) surface using density functional theory, J. Nanosci. Nanotechnol. 13 (2013) 3564–3567.
[29] J. Kim, J.-Y. Jo, I.-G. Choi, Y.-C. Kim, Search for adsorption geometry of precursor on surface using genetic algorithm: MoO_2Cl_2 on SiO_2 surface, J. Korean Ceram. Soc. 57 (2020) 669–675.
[30] Y. Kang, First-principles calculations of precursor adsorption on substrate during atomic layer deposition: the example of SiO_2 deposition using tris(dimethylamino) silane, Curr. Appl. Phys. 31 (2021) 228–231.
[31] N.-K. Yu, C.H. Moon, J. Park, H.-B.-R. Lee, B. Shong, Evaluation of silicon tetrahalide precursors for low-temperature thermal atomic layer deposition of silicon nitride, Appl. Surf. Sci. 565 (2021) 150603.
[32] T. Weckman, K. Laasonen, First principles study of the atomic layer deposition of alumina by TMA–H_2O-process, Phys. Chem. Chem. Phys. 17 (2015) 17322–17334.
[33] J. Lei, Y. Xie, A. Kutana, K.V. Bets, B.I. Yakobson, Salt-assisted MoS_2 growth: molecular mechanisms from the first principles, J. Am. Chem. Soc. 144 (2022) 7497–7503.
[34] J.E. Saal, S. Kirklin, M. Aykol, B. Meredig, C. Wolverton, Materials design and discovery with high-throughput density functional theory: the open quantum materials database (OQMD), J. Occup. Med. 65 (2013) 1501–1509.
[35] S. Kirklin, J.E. Saal, B. Meredig, A. Thompson, J.W. Doak, M. Aykol, S. Rühl, C. Wolverton, The open quantum materials database (OQMD): assessing the accuracy of DFT formation energies, npj Comput. Mater. 1 (2015) 15010.
[36] C. Arasa, P. Gamallo, R. Sayós, Adsorption of atomic oxygen and nitrogen at β-cristobalite (100): a density functional theory study, J. Phys. Chem. B 109 (2005) 14954–14964.
[37] P. Atkins, J. de Paula, Physical Chemistry, eighth ed., W. H. Freeman and Company, 2006.
[38] C.J. Cramer, Essentials of Computational Chemistry: Theories and Models, second ed., John Wiley & Sons, 2013.
[39] A. McQuarrie, Statistical Mechanics, University Science Book, CA, 2000.
[40] V. Wang, N. Xu, J.-C. Liu, G. Tang, W.-T. Geng, VASPKIT: a user-friendly interface facilitating high-throughput computing and analysis using VASP code, Comput. Phys. Commun. 267 (2021) 108033.
[41] K. van der Zouw, B.Y. van der Wel, A.A.I. Aarnink, R.A.M. Wolters, D. J. Gravesteijn, A.Y. Kovalgin, Low-resistivity molybdenum obtained by atomic layer deposition, J. Vac. Sci. Technol. A 41 (2023) 052402.
[42] G. Kresse, J. Hafner, Ab initio molecular dynamics for liquid metals, Phys. Rev. B 47 (1993) 558–561.
[43] G. Kresse, J. Furthmüller, Efficiency of ab-initio total energy calculations for metals and semiconductors using a plane-wave basis set, Comput. Mater. Sci. 6 (1996) 15–50.

[44] G. Kresse, D. Joubert, From ultrasoft pseudopotentials to the projector augmented-wave method, Phys. Rev. B 59 (1999) 1758–1775.
[45] P.E. Blöchl, Projector augmented-wave method, Phys. Rev. B 50 (1994) 17953–17979.
[46] J.P. Perdew, K. Burke, M. Ernzerhof, Generalized gradient approximation made simple, Phys. Rev. Lett. 77 (1996) 3865–3868.
[47] H.J. Monkhorst, J.D. Pack, Special points for Brillouin-zone integrations, Phys. Rev. B 13 (1976) 5188–5192.
[48] S. Grimme, J. Antony, S. Ehrlich, H. Krieg, A consistent and accurate ab initio parametrization of density functional dispersion correction (DFT-D) for the 94 elements H-Pu, J. Chem. Phys. 132 (2010) 154104.
[49] A. Togo, First-principles phonon calculations with phonopy and Phono3py, J. Phys. Soc. Jpn. 92 (2023) 012001.